Chapter 2

Cosmological Motivation

2.1 Introduction

This chapter summarizes the recent successes in CMB physics as well as the near-future polarization measurements that will be exciting but challenging. It is these prospects and challenges that ultimately motivated the detector development described in this thesis.

The standard model of cosmology and the theory of inflation are presented. The origin of the temperature and polarization anisotropies in the Cosmic Microwave Background are discussed in the context of these models as well as the cosmological parameters that have been or will be constrained by characterizing these anisotropies. Challenges associated with polarized foregrounds are also discussed.

2.2 Cosmological Expansion

There is strong observational evidence that the universe is expanding. Most notably, the distance between the Milky Way and neighboring galaxies is larger now than in the past, as evidenced by the spectral redshifting of distant galaxies relative to those nearby.

This expansion is well modeled by general relativity with the Friedmann-Walker-Robertson (FRW) metric:

$$ds^2 = -dt^2 + a(t)^2 \left[\frac{dr^2}{1 - Kr^2} + r^2(d\theta^2 + \sin^2\theta d\phi) \right] \tag{2.1}$$

where K is large scale curvature and $a(t)$ is the scale factor that records the history of the universe's dynamics. The scale factor vanished at the Big Bang and is currently unity (*Lyth* [1993]).

The time-time component of the Einstein Field Equation applied to the Equation 2.1 is commonly known as the Friedmann Equation:

$$\left(\frac{H(t)}{H_o} \right)^2 = \frac{\rho(t)}{\rho_o} - \frac{K}{a^2} \tag{2.2}$$

where the Hubble parameter $H(t) \equiv \dot{a}(t)/a(t)$ quantifies the expansion rate and is measured to currently be $H_o = 71 km\ s^{-1}\ Mpc^{-1}$. $\rho_o \equiv 3H_o^2/8\pi G$ is the critical density needed to close the universe; if our universes density exceeds ρ_o, it will ultimately re-collapse. In this chapter, the overdots in all equations denote a time derivative.

The energy density $\rho(t)$ is a sum of contributions from matter, radiation, and a cosmological constant whose individual densities change with time through the scale-factor. Conservation of the Stress-Energy Tensor ($T^\mu_{\nu;\mu} = 0$) formally establishes these dependencies, but the results are physically intuitive. The energy density of matter is the rest mass of each particle times its number density. This energy drops as the volume increases and is proportional to a^{-3}. Cosmic expansion not only dilutes photons like it does massive particles, but it also decreases the energy of each photon by an additional factor of a as expansion stretches the wavelengths. As a result, radiation density falls as a^{-4}. A cosmological constant is assumed to have an energy density that does not scale with a (*Carroll* [2003]). With these relationships in a flat universe, Equation 2.2 becomes:

$$H(t)^2 = H_o^2 \left(\Omega_m a^{-3} + \Omega_r a^{-4} + \Omega_\Lambda \right)$$

where Ω_* is the energy in a particular species normalized to the critical energy density ρ_o. During much of the universe's history, the energy density was dominated by one of these species and the other terms in the Freidmann equations could be ignored. As a result, the behavior during these epochs was

$$a(t) \propto \begin{cases} t^{1/2} & \text{radiation dominated} \\ t^{2/3} & \text{matter dominated} \\ e^{H_o t} & \Lambda \text{ dominated} \end{cases}$$

The very early universe was dominated by radiation, but transitioned into a matter dominated universe at $a_{eq} = 4.15 * 10^{-5}/(\Omega_m h^2)$. In more recent times, the universe has transitioned once again into one dominated by a poorly understood Dark Energy whose energy density appears to be nearly constant and whose negative pressure is causing the universe's expansion to accelerate. The best fit models to date describe Dark Energy as a cosmological constant (*Carroll* [2003]).

The average temperature of the universe is tied to the most populous particle, the photon, and this temperature has dropped as a^{-1} in step with the scaling of the photon energies. The high temperatures in the very early universe kept baryonic matter ionized and in tight thermal equilibrium with the photons through Thompson scattering. This statistical equilibrium between ionized gas (e.g. electrons and photons), photons, and neutral hydrogen atoms can be approximated by the Saha Equation:

$$\frac{X_e^2}{1 - X_e} \approx \frac{1}{n_b} \left[\left(\frac{m_e T}{2\pi} \right)^{3/2} e^{-|m_e + m_p - m_H|/T} \right]$$

where the $n_b = \eta_b n_\gamma \sim 10^{-9} T^3$ is the baryon number density (*Rybicki and Lightman* [1979]). X_e is the ratio of free electron number density to proton number density and the high temperatures of the early universe held X_e close to unity (all matter ionized). While energetics favored hydrogen production at temperatures of a few eV, the large number of photons in the Wien tail of the thermal distribution (large η_b) kept the universe ionized
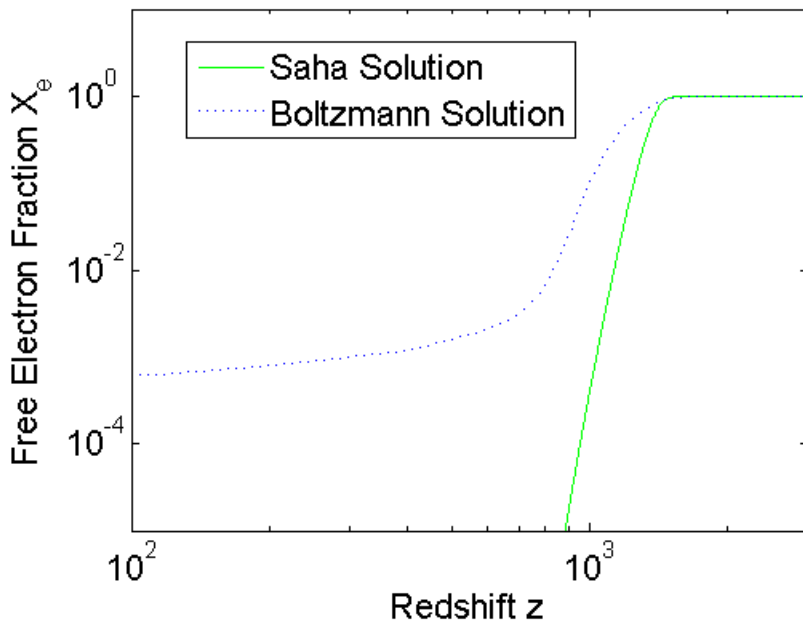
Figure 2.1. Free Electron fraction vs redshift for Equilibrium (Saha) and Non-equilibrium (Boltzmann) models. This figure is the result from an exercise from *Dodelson* [2003].

until $T \sim 0.25$eV, when X_e abruptly dropped and atomic hydrogen formed. This event is known as recombination and occurred at a redshift of $z = 1100$ (*Lyth* [1993]).

In reality, equilibrium between the photons and baryons was lost just before recombination in a phenomenon known as freeze-out where the Thompson scattering rate fell beneath the Hubble rate. Despite the lack of equilibrium, the Saha equation predicts a recombination redshift of $z \sim 1100$ in remarkable agreement with a more detailed numerical solution to the Boltzmann equation (See Figure 2.1) (*Dodelson* [2003]).

Subsequently, the photons freely streamed across the universe until they are seen in our telescopes today. Further expansion stretched their wavelength by a factor of 1100 into the millimeter range and this light source is known as the Cosmic Microwave Background (CMB). It is perhaps the most compelling evidence in favor of a hot Big Bang since once-competing "steady state" models of expansion had no natural way of explaining a near-uniform thermal radiation source at such a specific and high red-shift. Measurements by the Far InfraRed Absolute Spectrometer (FIRAS) instrument on the COsmic Background
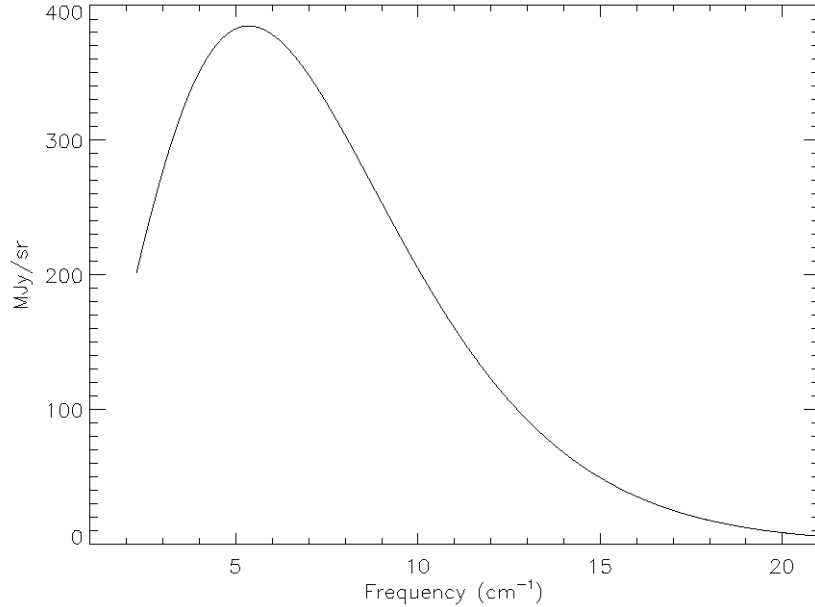
Figure 2.2. Frequency Spectrum measured by FIRAS. The data error-bars are famously smaller than the thickness of the theoretical co-plotted line. Figure from *Fixsen et al.* [1996]

Explorer (COBE) satellite have shown that it's frequency distribution is very closely modeled by a Plank Distribution (See Figure 2.2) that it is nearly isotropic, with temperature differences no larger than a few parts in 100,000 (*Fixsen et al.* [1996]).

2.3   Inflation

The Hot Big Bang scenario described in the previous section is well supported by measurements of the CMB and observations of Hubble's Law. In addition, predictions of the relative abundances of light elements (isotopes of Hydrogen and Helium) by Big Bang Nucleosynthesis agree well with the observed abundances in young galaxies (*Olive et al.* [2000]). Nonetheless, there are problems with the classic Hot Big Bang model.

Recent observations of the CMB anisotropies (see Section 2.5) suggest that the universe is nearly geometrically flat. Equivalently, the total energy density is very close to the critical

density, $\rho_c = 3m_{pl}^2 H_o^2 / 8\pi$, where m_{pl} is the Plank Mass. However, the Friedmann equation in a universe with curvature K can be rewritten as

$$\frac{|\rho(t) - \rho_c|}{\rho_c} = \frac{K}{(aH)^2} \propto t \tag{2.3}$$

where the proportionality applies to the early radiation dominated universe. For the current density to be $\rho_o \approx \rho_c$, the density at the plank scale temperatures would have to have been

$$\left| \frac{\rho(t_{plank})}{\rho_c} - 1 \right| \leq 10^{-59}$$

If this inequality was not met, the universe would have re-collapsed long before 13.7 Gyr, or it would have expanded so rapidly that it's average temperature would now be far lower than 2.7K. So the curvature of the very early universe must have been extremely close to flat. The hot big-bang model discussed above has no explanation for this required fine tuning (*Liddle* [1999]).

There are additional problems. The particle horizon is the maximum comoving distance that light could have traveled since the Big Bang:

$$\eta = \int_0^t \frac{dt}{a(t')} = \int_0^1 \frac{da'}{a'^2 H(a')}$$

Objects separated by distances larger than the horizon have never been in causal contact. The horizon has increased as the universe has aged and was much smaller at reionization than it is today; regions that were casually connected at $z \sim 1100$ now only subtend an angle of 1.12^o on the sky. Points currently separated by larger angles than this should not have been in causal contact at recombination and should never have thermally equilibrated. Nonetheless, the CMB has been measured to be isotropic on large angular scales to a level of 1 part in 100,000. Physics beyond the classic Big Bang universe is needed to explain this remarkable isotropy.

Inflation is a hypothesis that solves these and other related problems by speculating

that the universe underwent an accelerated superluminal expansion very shortly after the Big Bang. The horizon size can be rewritten as a logarithmic integral over the the Hubble Radius $1/aH$:

$$\eta(a) = \int_0^a d[ln(a')] \frac{1}{a'H(a')} \tag{2.4}$$

The Hubble radius is the distance that particles can travel over one expansion time (doubling of a); it defines the maximum separation between particles that are in causal contact at a specific time. When the early universe inflates, a sudden increase in a causes the Hubble radius to rapidly shrink. This allows for regions larger than the current universe's Hubble Radius to have once been causally connected and in thermal equilibrium, explaining the apparent isotropy observed in the CMB.

Since many inflation models are driven by scalar fields operating at temperatures of at least 10^{15} GeV, the scale factor at the end of inflation would have been $a_{end} \approx T_o/10^{15} GeV \approx 10^{-28} \approx e^{64}$. So to ensure that all scales currently within the horizon today were also once within the horizon before they were pushed out by inflation, inflation must have expanded the universe by at least 64 e-foldings. Such an expansion explains the high level of isotropy in the CMB between points on the sky that would not have been causally connected in the classic Big Bang scenario (See Figure 2.3). This rapid expansion also solves the flatness problem with almost identical numerology, where the 10^{28} decrease in Hubble radius in Equation 2.3 causes the difference between ρ and ρ_c to drop to the required 10^{-60} level (*Dodelson* [2003]).

The time-time and space-space components of the Einstein equations may be combined to give:

$$\ddot{a} = -\frac{4\pi G}{3}(\rho + 3P)$$

where the ρ and P are the energy density and Pressure of the fields driving inflation. The comovng Hubble radius will shrink ($\frac{d}{dt}\frac{1}{Ha} < 0$) when $\ddot{a} > 0$, or when the universe's expansion accelerates. This would have happened during inflation if the pressure P was
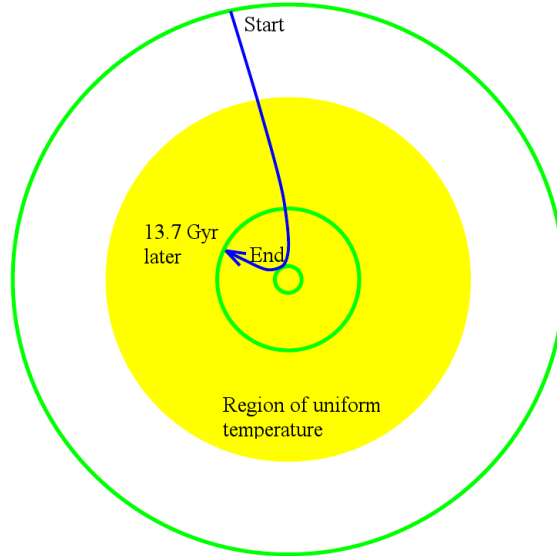
14

Figure 2.3. Cartoon showing how the Comoving Horizon (Hubble radius, Equation 2.4), pictorially shown by the green circles, shrinks between the Start and End of Inflation. Over the subsequent 13.7 Gyr, the our observable universe grows again, but not larger than the region of uniform temperature shown in yellow. This figure is adapted from a figure by Andrew Liddle (*Liddle* [1999]).

negative, specifically $P < -\rho/3$. Negative pressures arise when fields are trapped in a "false vacuum" with less Kinetic than Potential energy, allowing their difference, the pressure (T_i^i), to be negative.

While the detailed physics of inflation is not yet understood, many speculative models are driven by a scalar field potential $V(\phi)$ whose geometry is summarized by the slow roll parameters:

$$
\begin{aligned}
\epsilon &\equiv \frac{m_{Pl}^2}{2}\left(\frac{V'}{V}\right)^2 \\
\eta &\equiv m_{Pl}^2 \frac{V''}{V}
\end{aligned}
\tag{2.5}
$$

where $'$ denotes functional differentiation with respect to the field ϕ. Models frequently invoke the slow-roll approximation where $\epsilon << 1$ and $\eta << 1$, which ensures that inflation lasts long enough for the total scale expansion:

$$N \equiv \ln \frac{a_{end}}{a_{initial}} = \int_{t_i}^{t_e} H \, dt \cong -\frac{8\pi}{m_{pl}^2} \int_{\phi_i}^{\phi_e} \frac{V}{V'} d\phi$$

to exceed the required 64 e-foldings (*Liddle* [1999]).

2.4 Inflation as a Source of Structure

Inflation is not just a handy explanation for problems in the classic big bang model; it can also explain the origin of large scale structure in the universe. The gravitational ($g_{\mu\nu}$) and inflation ($\phi(x,t)$) fields have quantum mechanical fluctuations whose averages vanish, but whose variances do not. During inflation, the gravitational metric perturbations were amplified to cosmic scales outside the horizon where they are frozen in. The inflation field inflated too, but at the end we presume that it decayed into a hot bath of more familiar particles. These fields can be separated into homogeneous parts plus small fluctuations that are not spatially uniform:

$$\phi(x,t) = \phi_o(t) + \delta\phi(\mathbf{x},t)$$

$$
g_{\mu\nu} = \begin{pmatrix} -1 & 0 & 0 & 0 \\ 0 & a^2 & 0 & 0 \\ 0 & 0 & a^2 & 0 \\ 0 & 0 & 0 & a^2 \end{pmatrix} + 2 \begin{pmatrix} \Psi(\mathbf{x},t) & 0 & 0 & 0 \\ 0 & a^2\Phi(\mathbf{x},t) & 0 & 0 \\ 0 & 0 & a^2\Phi(\mathbf{x},t) & 0 \\ 0 & 0 & 0 & a^2\Phi(\mathbf{x},t) \end{pmatrix}
$$

$$
+ a^2 \begin{pmatrix} 0 & 0 & 0 & 0 \\ 0 & h_+(\mathbf{x},t) & h_\times(\mathbf{x},t) & 0 \\ 0 & h_\times(\mathbf{x},t) & -h_+(\mathbf{x},t) & 0 \\ 0 & 0 & 0 & 0 \end{pmatrix}
$$

where the first terms in these equations are the homogeneous parts (*Dodelson* [2003]). The metric tensor is given in rectangular coordinates for a flat universe with inhomogeneities

separated into the decoupled scalar and tensor terms. The tensor term is written only for modes traveling along the $\hat{z}$ axis. The space-space Einstein Equations to first order in $h_{+,\times}$ are:

$$h_{+,\times}^{\cdot\cdot} + 2\frac{\dot{a}}{a}h_{+,\times}^{\cdot} + k^2 h_{+,\times} = 0 \tag{2.6}$$

This equation of motion models tensor modes as a harmonic oscillator (gravity waves) with a damping term created by the expansion of the universe (*Carroll* [2003]). When quantized, the expectation of the variance is $\left\langle \hat{h}^{\dagger}(k,\eta)\hat{h}(k,\eta) \right\rangle \equiv (2\pi)^3 P_h(k)\delta^3(k-k')$, where

$$P_h(k) = \frac{8\pi}{k^3}\frac{H^2}{m_{plank}^2}|_{aH=k} \propto k^{n_T-3}$$

The last proportionality defines the tensor spectral index n_T, which is nominally 0 for an ideal scale invariant (Harrison-Zeldovich) power spectrum $k^3 P_h(k)$ (*Liddle* [1999]).

Perturbations to the scalar and inflations fields inflate as well, producing a similar scalar spectrum $P_{\delta\Phi}$. However, the two fields couple as they are pushed out of the horizon, which complicated the mathematics considerably (*Dodelson* [2003]). The result of this analysis is that:

$$P_{\Phi}(k) = \frac{8\pi}{9k^3}\frac{H^2}{\epsilon m_{plank}^2}|_{aH=k} \propto \frac{1}{k^3}\left(\frac{k}{H_o}\right)^{n_S-1} \tag{2.7}$$

(*Liddle* [1999]). As above, the scalar spectral index n_S is nominally 1 for a scale invariant spectrum. COBE fixed the magnitude of the scalar spectrum on large scales at $\delta_H \sim 2 \times 10^{-5}$, which from Equation 2.7 fixes the energy scale of inflation to be similar to energy scales associated with GUT scales:

$$V^{1/4} \sim \epsilon^{1/4} 10^{16} GeV$$

While ϵ and η are the more fundamental parameters that characterize the inflationary

17

potential's shape, the figures n_S and n_T are more closely tied to observations and are often preferred in the observational literature. Logarithmic derivatives of the above spectra establish relationships between them:

$$n_S = 1 - 6\epsilon + 2\eta$$

$$n_T = -2\epsilon$$

Additionally, the tensor to scalar ratio defined in terms of CMB anisotropy C_ls can be shown to be

$$r \equiv \frac{C_l^T}{C_l^s} \cong 4\pi\epsilon$$

A successful measurement of r could constrain the energy scale of inflation and restrict the space of viable models for the inflationary potential (*Liddle* [1999]). Data from Large Scale Structure surveys and CMB maps have already constrained n_S and hence some inflationary potentials (see Figure 2.4). The space of viable models will no doubt decrease with improved measurements of the Microwave Background.

Finally, the two parameters ϵ and η suffice to summarize all slow roll inflation potentials, while the extra parameter in the set n_S, n_T, and r contais no new information. Eliminating n_S leads to a constancy relationship:

$$r = -2\pi n_T$$

This constancy relationship is generally true of *all* slow roll inflation potentials. Our field has yet to develop the means to measure a non-zero r, let alone n_T to test this relationship. However, it is unlikely that any mechanism other than slow roll inflation would relate the two spectra in this specific way. Detecting scalar and tensor perturbations with this relationship would constitute (for many scientists) a "smoking gun" confirmation of the inflationary paradigm.
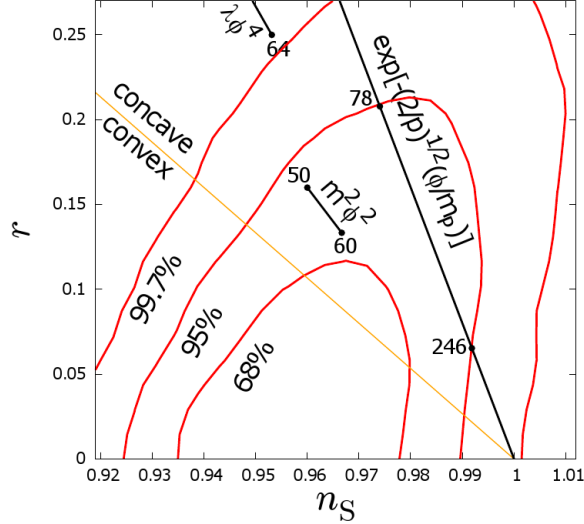
Figure 2.4. Large Scale structure data from Sloan Digital Sky Survey as well as CMB data from WMAP, ACBAR, QUAD, and BICEP constrain $r < 0.17$ and $n = 0.926 \pm 0.026$ a 95% confidence. Confidence contours are co-plotted with different inflation models, where the labeled points refer to the number of e-foldings. These data alread rule out a chaotic potential $\lambda \phi^4$ to high confidance. Figure from *Finelli et al.* [2010].

2.5 Temperature Anisotropies in the Microwave Background

The Microwave Background is not perfectly uniform in temperature; there are variations of 1 part in 100,000. These anisotropies are sourced by the metric perturbations discussed in the previous section and their time-evolution is modeled by the Boltzmann Equations. The Boltzmann Equations relate the statistical distribution of particles in different momentum states to the collision rates between these particles in a general way that does not require statistical equilibrium. A full discussion of this theory is beyond the scope of this thesis, and we just summarize results as needed in the remaining sections. We refer the interested reader to *Dodelson* [2003] and *Liddle and Lyth* [2000].

The Boltzmann Equations for the photons' anisotropic temperature $T(x, p, \eta) = T(\eta)[1 + \Theta(x, \hat{p})]$ are often decomposed into equations for different multipole moments:

$$\Theta_\ell \equiv \frac{1}{-i^\ell} \int_{-1}^{1} \frac{d\mu}{2} \mathcal{P}_\ell(\mu) \Theta(\mu)$$

19

where μ is the cosine of the angle between the wavenumber of the perturbation mode under consideration and direction of photon propagation and $\mathcal{P}_\ell$ is a Legendre Polynomial of order ℓ. For $\ell \geq 2$, the Boltzmann equations can be approximated as

$$\dot{\Theta}_\ell - \frac{k\ell}{2\ell + 1}\Theta_{\ell-1} + \frac{k(\ell + 1)}{2\ell + 1}\Theta_{\ell+1} = \dot{\tau}\Theta_\ell \qquad (2.8)$$

(*Hu and Dodelson* [2002]). Prior to recombination, the photons were tightly coupled to the electrons and nuclei. This era was characterized by photons having a mean free path much smaller than the Hubble radius ($\tau >> 1$), which suppresses the first and third terms of Equation 2.8, forcing $\Theta_\ell \sim \Theta_{\ell-1}/\tau$. As a result, only the first two moments were relevant before recombination. Combining the equations for the first two moments with a Boltzmann equation for the velocity of baryonic matter gives an equation for the photon monopole that is analogous to a driven and damped mechanical harmonic oscillator:

$$\left\{\frac{d^2}{d\eta^2} + \frac{\dot{R}}{1+R}\frac{d}{d\eta} + k^2 c_s^2\right\}[\Theta_o + \Phi] = \frac{k^2}{3}\left[\frac{1}{1+R}\Phi - \Psi\right] \qquad (2.9)$$

where $R = 3\rho_b/4\rho_\gamma$ is the ratio of baryons to photons and $c_s = 1/\sqrt{3(1+R)}$ is the sound speed through the photon-baryon fluid (*Hu and Dodelson* [2002]). The combination of $\Theta_o + \Psi$ more closely relates to the observed temperatures than just Θ_o since the photons redshift as they climb out of the wells with a potential -Ψ.

Equation 2.9 says that modes of wavenumber k oscillate with a restoring force provided by the photon pressure (third term LHS) acting on the ionized baryonic matter while the gravitational wells assist compression (RHS). Inflation excites all modes with the same phase, so the most important are the harmonics reaching full compression or rarification at recombination; they are the modes that provide the CMB anisotropies with the greatest power. The age of the universe at recombination and the sound speed c_s determine the wavenumbers of these resonant modes. Cosmologies with higher baryon densities (larger R) will have lower sound speeds and hence lower wavenumber peaks in $\Theta_o + \Psi$.

The tight coupling approximation applies only to the largest scale modes. Over a Hubble time H^{-1}, the photons random walk a distance of

$$\lambda_D \sim 1/\sqrt{n_e \sigma_T H}$$

where σ_T is the scattering cross section and n_e the number density of electrons. Modes with wavelengths smaller than this are washed out, and so only the first few lowest wavenumber modes leave an observable imprint on the microwave background (*Dodelson* [2003]).

After recombination, the photons decouple from the baryonic matter and free-stream across the universe. Since $\tau \ll 1$ in a neutral universe, all terms of Equation 2.8 are relevant, and power leaks out of the first two multipoles and into the higher ℓ modes. Simply put, the modes with wavenumber k at recombination manifest themselves today as angular anisotropies with scale $\ell \sim k\eta_o$, where η_o is the Hubble radius of the last scattering surface. Cosmologists often resolve the observed photon energy into a basis of spherical harmonics:

$$\Theta(x, p, \eta) = \sum_{l=1}^{\infty} \sum_{m=-l}^{\ell} a_{\ell m}(x, \eta) Y_{\ell m}(p)$$

The coefficients' average should vanish $\langle a_{\ell m} \rangle = 0$, but the variance for a specific ℓ should not:

$$\langle a_{\ell m} a^*_{\ell' m'} \rangle = \delta_{\ell \ell'} \delta_{mm'} C_\ell$$

2.6 Parameters constrained by Temperature Anisotropies

Numerous experiments have measured the temperature anisotropies, and the results from WMAP and are shown in Figures 2.5 (*Larson et al.* [2010a]). The angular power spectrum has a series of pronounced harmonic peaks that are difficult to explain outside of an inflationary scenario. These measurements have had a profound influence on our understanding of the cosmos, allowing scientists to constrain multiple cosmological parameters
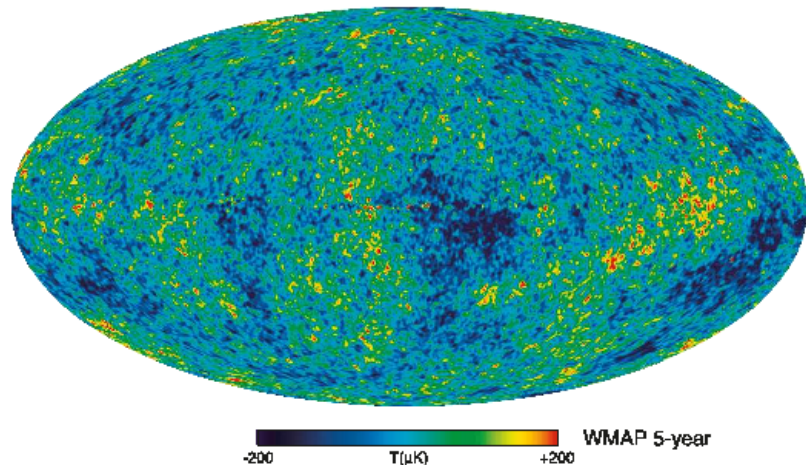
Figure 2.5. WMAP's full sky false color map of deviations in temperature from the 2.71K average. Figure from *Larson et al.* [2010a]

summarized in Table 2.1 (*Komatsu et al.* [2010]). While this is accomplished through like-lihood estimators, many of the parameters have an intuitive connections to the features of the spectrum in Figure 2.6.

2.6.1 Curvature

The CMB has been used to demonstrate that the universe is geometrically flat on the largest observable scales. Were the universe not flat, rays that were initially parallel would converge or diverge and the original inhomogeneities discussed in the previous section would be projected onto respectively smaller or larger angular scales. The first anisotropy peak sits at $\ell \sim 200$, which is consistent with a flat Universe with $\Omega_K = 0$ and implies, from the Friedmann Equation, that the universe has a critical density ρ_c. The flatness of the universe is one of the key predictions of inflation confirmed by the CMB's angular power spectrum.
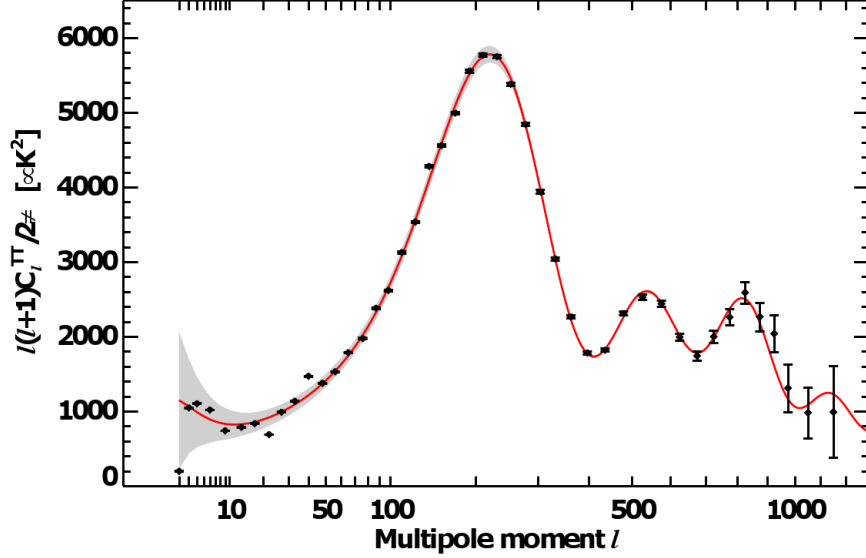
Figure 2.6. CMB Temperature Angular Power Spectrum of the full sky from seven years of WMAP data. This plots variance of spot temperature vs reciprocal of spot size Figure from *Larson et al.* [2010a].

2.6.2 Baryon Density

The right-hand side of Equation 2.9 is a driving term that introduces a particular solution in addition to the homogeneous terms, causing an offset to the zero point of oscillations. Since the observed temperature fluctuations are proportional to the variance of $\Theta_o + \Psi$, this offset will enhance the odd peaks while suppressing the even ones. This effect will be stronger for lower resonant wavenumbers, and hence larger values of R.

As a result, the ratio of the heights of the even and odd peaks can be used to constrain R. Since the photon density is tightly constrained by the CMB temperature, the baryon density was thus determined to be $\Omega_b = 0.0449 \pm 0.00288$. This figure is consistent with measured deuterium abundances in high redshift quasars when compared against the theory of Big Bang Nucleosynthesis, but it places an even tighter constraint than those measurements.

2.6.3 Matter Density

A cosmology with a low matter density will have an epoch of matter-radiation equality that is closer to recombination. Since the photons are neither able to cluster nor help gravitational wells grow, those gravitational modes that re-enter the horizon long before recombination decay away. The photons that compress into such a decaying gravitational well will see a lowered potential barrier when they rarify and can emerge much hotter. This effect results in enhanced power in the smaller acoustic peaks for lower matter density and has been used to constrain $\Omega_{CDM} = 0.222 \pm 0.026$.

2.6.4 Scalar Spectral Index

Equation 2.7 defines the scalar spectral index, where a scale-invariant power would correspond to $n_S = 1$. If $n_S < 1$, then the power in the gravitational wells, and hence the CMB anisotropies, will be smaller at small scales resulting in a tilt to the spectrum. Since the spectrum is often normalized around a point point of $\ell = 10$, this effect becomes very pronounced at the high-ℓ end of the spectrum focused on by ACBAR. By assuming that there is no running scalar-index (i.e, n_s is not a function of k), WMAP and ACBAR data constrain $n_S = 0.964 \pm 0.0114$ (*Komatsu et al.* [2010]).

Table 2.1. Parameters constrained from 7-year WMAP data set

| Parameter	Fit	Description
$100\Omega_b h^2$	$2.258^{+0.057}_{-0.056}$	Baryon density
$\Omega_{CDM}h^2$	0.1109 ± 0.0056	Cold Dark Matter density
Ω_Λ	0.734 ± 0.029	Dark Energy density
Ω_k	$0.080^{+0.071}_{-0.093}$	Curvature density
n_S	0.964 ± 0.0114	Scalar Spectral Index
r	< 0.36 (95% CL)	Tensor Scalar Ratio
Σm_ν	$< 1.3eV$ (95% CL)	Neutrino mass sum
t_o	13.75 ± 0.13 Gyr	Current Age of the Universe
H_o	71.0 ± 2.5 km/s/Mpc	Current Hubble Parameter, $H = 100h$
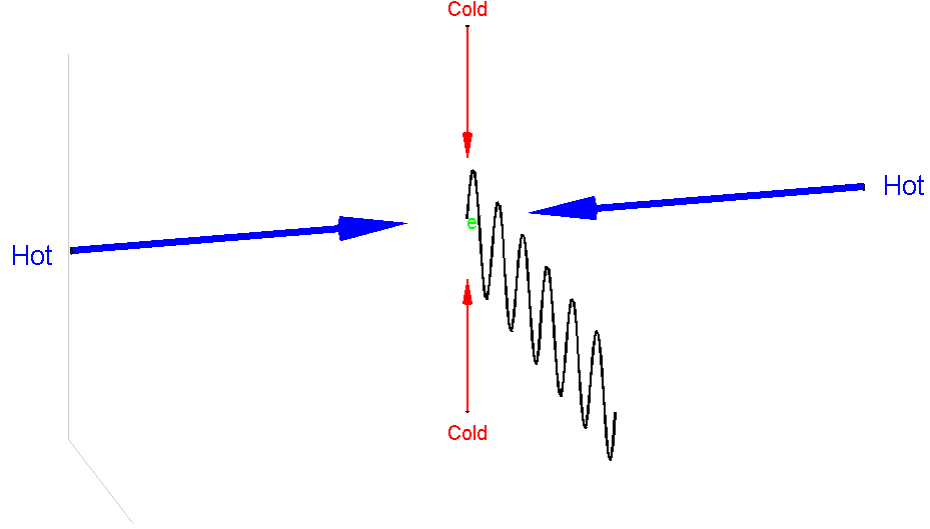
Figure 2.7. A Cartoon illustrating how Thomson scattering can convert a quadrupolar temperature distribution into polarized signal. In this case, the hot regions (blue) on the left and right drive the electron in vertical oscillations harder than the cooler region (red) above and below drive horizontal oscillations, resulting in scattered radiation that is partially polarized in the vertical, as depicted in black This figure is adapted from one in *Hu and White* [1997].

2.7 E mode Polarization Anisotropies

The Microwave Background is also polarized and mapping this is now the primary occupation in our field. This polarization arises because the CMB photons Thomson scatter off the primordial plasma. A photon traveling in the direction $\hat{n}^{inc}$ with polarization $\hat{\epsilon}(\hat{n}^{inc})$ will scatter off charged particles into the direction $\hat{n}$ and polarization $\hat{\epsilon}(\hat{n})$ with a cross section proportional to

$$\sum_{j=1}^{2} |\epsilon_i(\hat{n^{inc}})\epsilon_j(\hat{n})|^2 \tag{2.10}$$

(*Rybicki and Lightman* [1979]). Figure 2.7 shows a cartoons that is often cited to intuitively explain how polarization arises from Thomson scattering (*Hu and White* [1997]). If a scattering particle is illuminated uniformly, it will scatter unpolarized light. But if it is illuminated with hot sources along the $\hat{x}$ axis, but cool along the $\hat{y}$ axis, it will scatter light with a vertical partial polarization.

The polarization of light with wavevector in the $\hat{z}$ direction is characterized by the Stokes parameters (*Rybicki and Lightman* [1979]):

$$
\begin{aligned}
I &\equiv E_x^2 + E_y^2 \\
Q &\equiv E_x^2 - E_y^2 \\
U &\equiv E_{x+y}^2 - E_{x-y}^2 \\
V &\equiv E_{x+iy}^2 - E_{x-iy}^2
\end{aligned}
\tag{2.11}
$$

I is simply the intensity. Q is the difference in power polarized along $\hat{x}$ and $\hat{y}$ while U is that difference in power polarized on the pair of axis rotated 45° from $\hat{x}$. These characterize the magnitude and orientation of linear polarization. V quantifies how circular the polarization is by differencing the two chiralities. Thompson Scattering should not produce circular polarizations, so V is expected to be zero.

Let the incident light upon a scattering particle have a temperature distribution $\Theta(k, \hat{k} \cdot \hat{n}^{inc})$, where k is the wavevector of a single acoustic mode. If we are positioned such that we only see light scattered in the $\hat{n} = \hat{z}$ direction, inserting Equation 2.10 into Equations 2.11:

$$
\begin{pmatrix} Q \\ U \end{pmatrix} \propto \int d\Omega' \Theta(n') \sum_{j=1}^{2} \begin{pmatrix} \left|\hat{x} \cdot \hat{\epsilon}_j'\right|^2 - \left|\hat{y} \cdot \hat{\epsilon}_j'\right|^2 \\ \left|(\hat{x}+\hat{y}) \cdot \hat{\epsilon}_j'\right|^2 - \left|(\hat{x}-\hat{y}) \cdot \hat{\epsilon}_j'\right|^2 \end{pmatrix}
\tag{2.12}
$$

$$
\propto \int d\Omega' \Theta(n') \begin{pmatrix} Y_{2,2}(\theta', \phi') + Y_{2,-2}(\theta', \phi') \\ Y_{2,2}(\theta', \phi') - Y_{2,-2}(\theta', \phi') \end{pmatrix}
\tag{2.13}
$$

which vanishes for all multipole moments of $\Theta(n')$ aside from $\ell = 2$ (*Kosowsky* [1996]). For a scalar mode traveling with a wavenumber in the $\hat{x}$ axis, the relevant moment is

$$
\Theta(k, k \cdot \hat{n}^{inc}) \propto \Theta_2(k) \mathcal{P}_2(\hat{k} \cdot \hat{n}^{inc})
\tag{2.14}
$$

So $Q(\hat{(z)}, k) \propto \Theta_2(k)$ and $U(\hat{z}, k) = 0$ in that specific situation. More generally, the
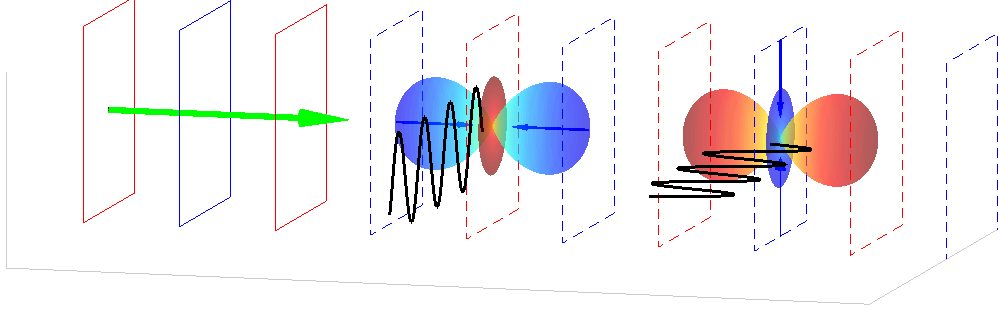
Figure 2.8. Cartoon illustrating E-mode polarization from a single fourier mode of scalar perturbation. Cool regions are red, hot are blue and the blue arrows represent the strongest incident optical power onto the charged particle. The scattered light is partially polarized, and the wave of the strongest polarization is depicted in black. Note that this must be either parallel or perpendicular to the wavevector (green) and hence the temperature gradient.

stokes parameters of photons scattering off a scalar mode traveling in the direction $\hat{k} = (\sin(\theta_k)\cos(\phi_k), \sin(\theta_k)\sin(\phi_k), \cos(\theta_k))$ are

$$\begin{pmatrix} Q \\ U \end{pmatrix} \propto (1 - (\hat{n} \cdot \hat{k}))^2 \Theta_2(k) \begin{pmatrix} \cos(2\phi_k) \\ \sin(2\phi_k) \end{pmatrix} \equiv \Theta_p(\hat{n} \cdot \hat{k}) \begin{pmatrix} \cos(2\phi_k) \\ \sin(2\phi_k) \end{pmatrix} \qquad (2.15)$$

Just like the temperature anisotropies, the full distribution of polarized light $\Theta_P(k, \mu)$ is governed by a Boltzmann Equation. In the strong coupling limit, this reduces to the qradrupole distribution in Equation 2.14. After recombination, power from $\ell = 2$ leaks into the higher-ℓ anisotropies

$$\Theta_{P\ell}(k) \simeq -\frac{5k\Theta_1(k, \eta_*)\ell^2 j_\ell(k\eta_o)}{6\dot{\tau}(k\eta_o)^2} \qquad (2.16)$$

(*Kosowsky* [1996]). The key feature of this distribution is that the orientation of the polarization is always parallel or perpendicular to the gradient in temperature, as illustrated in Figure 2.8. After a parity flip, the polarization is still be parallel or perpendicular to that gradient: the pattern is even under parity. Since there is no directional information to a scalar mode aside from it's own wavevector, the scattered light has no choice but to be polarized parallel or perpendicular to these directions, and this property is preserved even after the photons free-stream and move power into the higher ℓ modes in Equation 2.16.
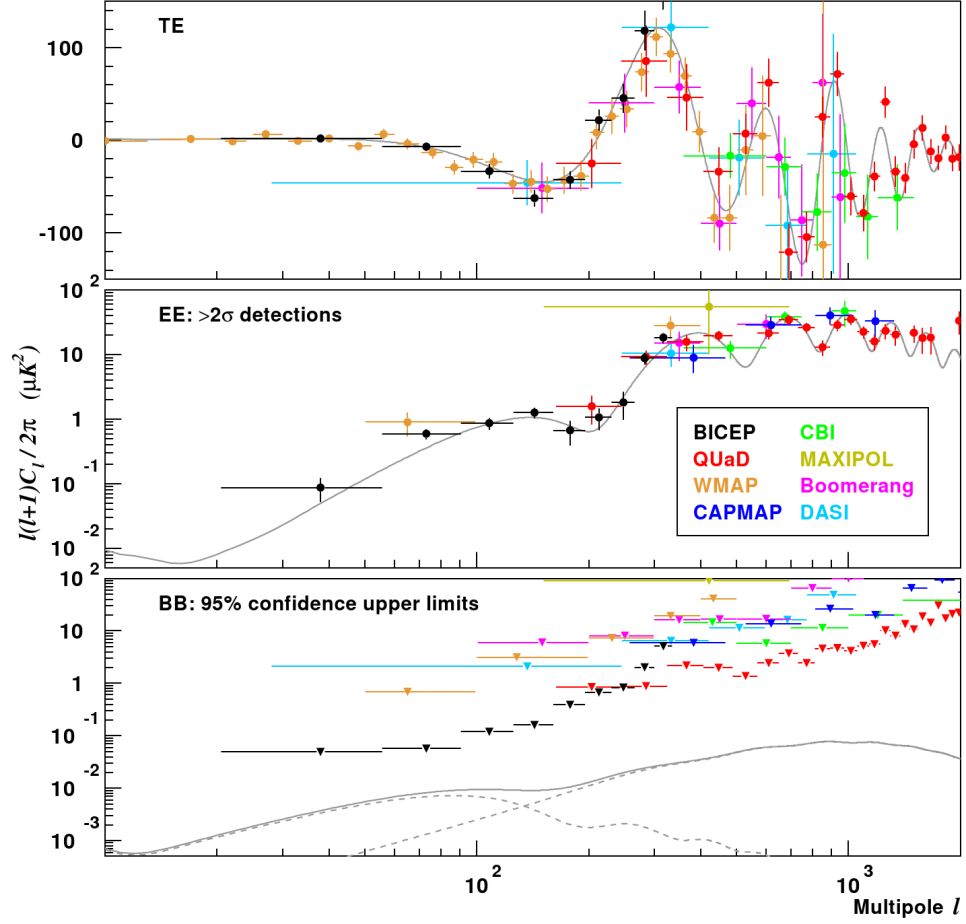
Figure 2.9. E-mode Angular Power Spectra from several experiments. Figure from *Chiang et al.* [2010].

The E-mode/B-mode decomposition reveals this underlying even-symmetry:

$$E(\ell) \equiv Q(\ell)\cos(2\phi_\ell) + U(\ell)\sin(2\phi_\ell)$$

$$B(\ell) \equiv -Q(\ell)\sin(2\phi_\ell) + U(\ell)\cos(2\phi_\ell)$$

where in this equation, ℓ is a vector projected on the sky making an angle ϕ_ℓ with respect to the $\hat{x}$-axis. For the even symmetry scalar mode generated patterns, $C_{BB}(\ell) = 0$ and $\lim_{\ell \gg 1} C_{EE}(\ell) = C_{P,\ell}$ (*Challinor and Peiris* [2009]). Recently, several experiments have measured these spectra as shown in Figure 2.9.

The EE spectra, particularly those measured by BICEP and QUAD, show similar fring-

ing as the temperature spectrum (Figure 2.6). However, the dipole moment at recombination primarily sourced the E-modes, in constrast the temperature anisotropies that were sourced by both monopole and dipole terms. As a result, the E-modes are a half-cycle out of phase from the temperature peaks, as revealed in the TE correlation spectrum. And because E-modes are only sourced by one moment, the peaks have a higher fractional power compared to the Temperature. Additionally, it's power is lower by an order of magnitude because the multipole moments at recombination drop by factors of $\dot{\tau}$ for each increase in ℓ. Finally, the B-mode power spectrum is consistent with zero, as predicted by the spectrum sourced by scalar perturbations.

2.8   B mode Polarization Anisotropies

Scalar modes are not the only polarization source in the CMB. Tensor perturbations also generate temperature quadrupole moments, but unlike the scalar perturbations, they have their own $(h_+, h_\times)$ polarization as well. This additional structure that is absent from the scalar modes allows the polarized photons to scatter into both even and odd parity patterns, as illustrated in the cartoons in Figure 2.10.

Photons were incident upon particles at last-scattering from all directions $\hat{n}^{inc} = (\sin(\theta)\cos(\phi), \sin(\theta)\sin(\phi), \cos(\theta))$. A tensor mode traveling in the $\hat{z}$ direction with polarization $h_\times$ has an angular dependence

$$\Theta^T \propto \sin^2(\theta)\sin(2\phi) = 2n_x^{inc}n_y^{inc}$$

For a gravity wave propagating in the general direction $(\sin(\theta_k)\cos(\phi_k), \sin(\theta_k)\sin(\phi_k), \cos(\theta_k))$, the general temperature distributions is just the result of rotating the $\hat{n}^{inc}$ by a matrix $\tilde{R}$ that would put $\hat{k}$ back along the $\hat{z}$ axis.
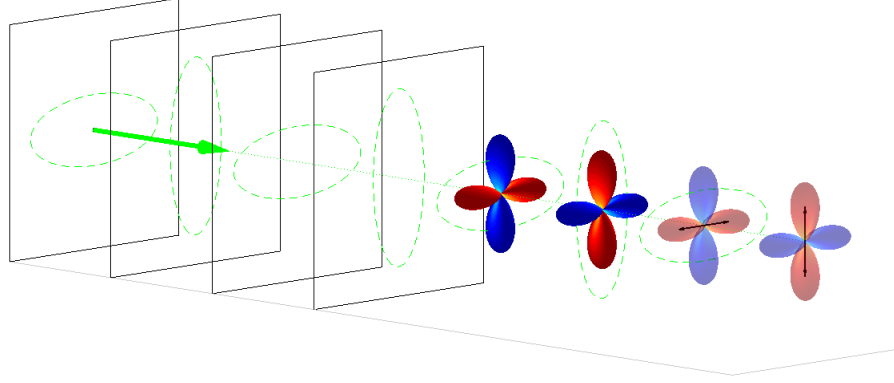
(a) E-modes from h_+ Gravity waves
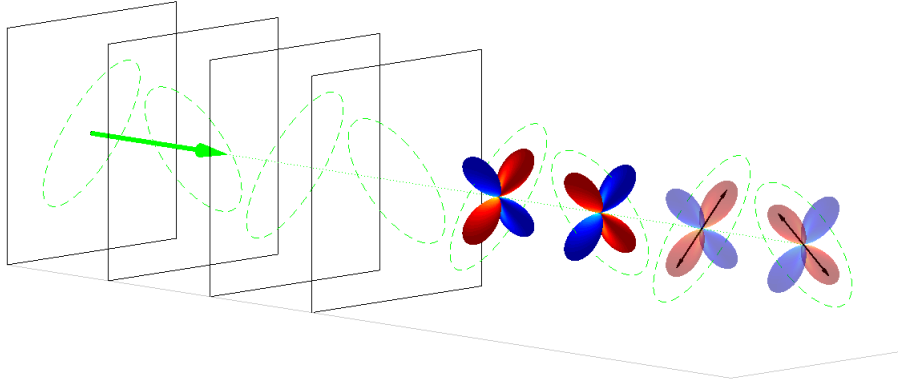
(b) B-modes from $h_\times$ Gravity Waves

Figure 2.10. Cartoons illustrating E-mode and B-mode polarization from a single fourier modes of tensor perturbations (gravity waves). Cool regions are red, hot are blue. The axis with the highest amplitude of electron oscillation is denoted with the double-headed black arrows. This will be the plane of oscillation, projected onto the sky. Note that in 2.10(b), the polarization is at a 45° angle to the wavevector (in green) and hence temperature gradient. This Figure is adapted from one in *Kovac* [2004].

$$
\begin{aligned}
\Theta^T &\propto (\tilde{R}n^{inc})_x (\tilde{R}n^{inc})_y \\
&\propto \cos(\theta_k) \left[e^{-i2\phi_k} Y_{2,-2}^*(\theta,\phi) - e^{i2\phi_k} Y_{2,2}^*(\theta,\phi) \right] + \\
&\quad \sin(\theta_k) \left[e^{-i\phi_k} Y_{2,-1}^*(\theta,\phi) - e^{i\phi_k} Y_{2,1}^*(\theta,\phi) \right]
\end{aligned}
$$

(*Dodelson* [2003]). From Equation 2.13, the Q and U components pick out only the $m = 2$ Harmonics, yielding

$$
\begin{pmatrix} Q \\ U \end{pmatrix} \propto \Theta_0^T(k)\cos(\theta_k) \begin{pmatrix} -\sin(2\phi_k) \\ \cos(2\phi_k) \end{pmatrix} \simeq \Theta_0^T(k)\hat{n}\cdot\hat{k} \begin{pmatrix} -\sin(2\phi_k) \\ \cos(2\phi_k) \end{pmatrix}
$$

This results in a pure B-mode signal, one who's polarization is oriented 45° from the intensity gradient. A similar analysis of h_+ polarized gravity waves would yield a pure E-mode contribution:

$$
\begin{pmatrix} E \\ B \end{pmatrix} \propto \hat{n}\cdot\hat{k} \begin{pmatrix} h_+ \\ h_\times \end{pmatrix}
$$

When a tensor perturbation re-enters the horizon, causal physics described by Equation 2.6 determine it's time evolution. The second term sourced by the Universe's expansion acts as a damping term and the waves rapidly decay away. As a result, there should be a strong peak in the B-mode anisotropy spectrum corresponding to the modes that were just re-entering the horizon at recombination and greatly suppressed power at other angular scales (see Figure 2.11). Additionally, the effects of Tensor perturbations on the Temperature power spectrum are degenerate with the Scalar perturbations. However, this B-mode signature cannot be produced by Scalar modes and can in principle be used to determine the tensor-to-scalar ratio r. As of the writing of this thesis, non-zero CMB B-modes have not been detected.

2.9   Gravitational Lensing

The CMB should be distorted by gravitational wells between us and the last scattering surface by lensing. Following an order of magnitude calculation from Lewis and Chanllinor (*Lewis and Challinor* [2006]), the impact on the temperature power spectrum will be minor. If only point sources of well depth 3×10^{-5} lens the CMB photons, then they will be deflected $\delta\alpha \sim 4\Psi \sim 1.2 \times 10^{-4}$. Since the matter power spectrum suggests that most of these wells have a comoving diameter of $\sim$ 150 Mpc, there should be around 100 such wells between us and the last scattering surface 14000 Mpc away. So the total random walk of the CMB
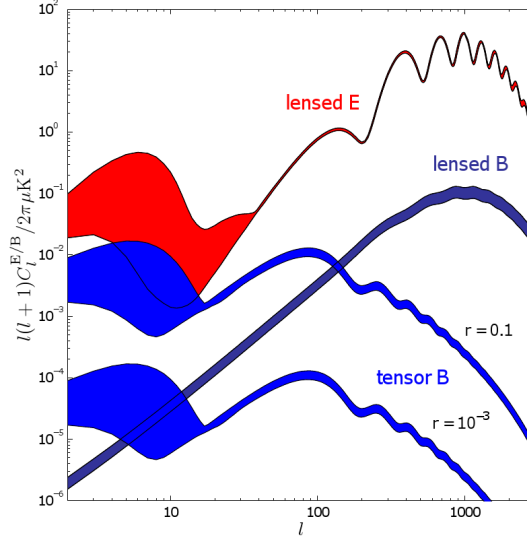
Figure 2.11. Simulated E-mode and B-mode angular power spectra. The lensing B-modes (see section 2.9) are separated from the primordial B-modes with $r = 0.1$ and $r = 10^{-3}$ possibilities. These were compiled with data available in 2006, displaying the 95% confidence intervals. Figure from *Lewis and Challinor* [2006].

photons will experience a total deflection of $\sqrt{10} \times 1.2 \times 10^{-4} \sim 1 \times 10^{-3}$ rad, or roughly 3 arcmin. This means that the lensing contribution only dominates on scales in excess of $\ell \sim 2000$. Lensing can have a subtle impact on the acoustic peaks because, for lensing sources half-way to last-scattering, the lensing will be correlated on scales $150/7000$ rad $\sim 1.2^{o}$. This effect distorts the anisotropies at a $0.05^{o}/1.2^{o} \sim 2.5\%$ which will widen the accoustic peaks at the percent level.

However, lensing will have a more pronounced impact on the polarization. Lensing will distort the CMB photons' propagation direction by $d = \nabla \phi$, where the well-known lensing potential can be written as an integral over the gravitational potentials $\Psi(z)$:

$$\phi = 2 \int_0^{z_{CMB}} \frac{dz}{H(z)} \frac{\chi(z) - \chi(z_{CMB})}{\chi(z)\chi(z_{CMB})} \Psi(z)$$

and where $\chi(z)$ is the comoving distance to a lensing well at redshift z. The stokes parameters will be modified by $X(\hat{n}') = X(\hat{n} + d)$, where X can be I, Q, or U. Even though lensing will not mix Q and U, it will shear E into B and vise versa (*Lewis and Challinor*
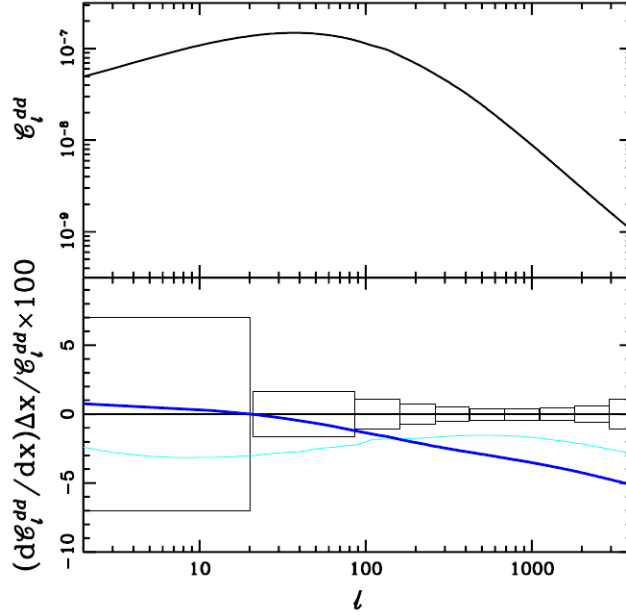
Figure 2.12. Simulated angular power spectrum for the lensing deflection angle $C_\ell^{dd} \equiv \ell(\ell+1)C_\ell^{phi}$. The top panel is simulated for $m_\nu = 0$ while the bottom shows deviations for $\Delta m_\nu = 0.1$ eV and $\Delta w = 0.2$. Figure from *Kaplinghat et al.* [2003]

[2006]). In particular, the much hotter E-modes will be partially reprocessed into B-modes with an angular power spectrum

$$C_\ell^B = \int \frac{d^2\ell'}{(2\pi)^2} \left[\ell'(\ell-\ell')\right]^2 C_{|\ell-\ell'|}^\phi C_{|\ell'|}^E sin^2 2(\theta'_\ell - \theta_\ell) \tag{2.17}$$

where C^{phi} is the angular power spectrum of the lensing potential. This results in a lensing B-mode contribution shown in Figure 2.11 ((*Lewis and Challinor* [2006])).

While this may dominate over the primordial B-modes for many possible values of r, it will likely be scientifically interesting in it's own right. The lensing signal should be sensitive to parameters that impact structure formation late in our universes history, specifically the sum of the three generations of neutrino masses and the dark energy equation of state.

Figure 2.12 shows the simulated power spectrum for the lensing deflection angle as well as distortions from a change in total neutrino mass Δm_ν=0.1eV and the dark energy equation of state Δw=0.2. Massive neutrinos do not cluster on scales smaller than their Jean's length, which decreases as the universe cools. However, we do expect neutrinos to

33

cluster at scales larger than their jean's length at matter-radiation equality, which results in a slight decrement of power at high-ℓ.

Conversely, dark energy drives cosmic acceleration and suppresses structure at late times. As a result, it will suppress the deflection angle power spectrum more at low-ℓ. These two effects are sufficiently distinct that they may be simultaneously constrained by measurements of the lensing B-mode signature (*Kaplinghat et al.* [2003]).

The primordial B-modes will likely be dominated by lensing, but there are several proposals to mitigate this possibility should it arise. Maps that cover large portions of the sky from Plank and SPIDER may be sensitive to the B-mode reioniation peak at $\ell \sim 7$ where lensing is very weak. Additionally, the lensing statistics is non-gaussian, as seen from Equation 2.17 that convolves two gaussian distributions. There are several proposals that exploit this non-gausianity of the lensing distribution to statistically de-lens maps and possibly allow for detection of B-modes at the reionization peak even if r is very small.

2.10 Polarized Galactic Foregrounds

Efforts to detect B-mode polarization will likely be confounded by contamination from polarized galactic foregrounds. As of the writing of this thesis, few CMB experiments have had to remove these sources, but that may change in the near future as we seek to map the sky's millimeter polarization to even finer levels. Synchrotron emissions and thermal dust emissions are most likely the strongest foreground sources. Fortunately, they bear different spectral signatures than the CMB's 2.7K blackbody spectrum, so in principle, they can be characterized and removed from millimeter-wavelength maps if the sky is mapped at multiple frequency channels. For a foreground model with N components, an experiment will need at least $N + 1$ channels to remove the foregrounds from a CMB map. The spectral properties of synchrotron and thermal dust emissions are summarized in the next two subsections.

2.10.1 Synchrotron Emission

Synchrotron radiation is emitted by cosmic rays that are accelerated by the galactic magnetic field. The antenna temperature of these emissions is $T(\nu) \propto \nu^{\beta}$, where the exponent $\beta = -(p+3)/2$ is related to the power law for electron energies $N(E) \propto E^{-p}$. Synchrotron radiation can have a strong fractional partial polarization of

$$f = \frac{p+1}{p+7/3}$$

aligned with the magnetic field lines. For microwave frequencies with $\beta \approx -3$, this can be as high as 0.75, but line of sight averaging tends to reduce this significantly.

Mapping this foreground in the millimeter spectral range is still an active area of research, but the WMAP satellite has contributed significantly to our understanding of it. WMAP mapped the sky at five spectral bands spanning a microwave/millimeter range of 23GHz to 94GHz. For coarse 3.7^o pixels, the dominant polarization was consistent with a Synchrotron source with $\beta \approx -3$ (See figure 2.13). The precise synchrotron spectral index varied with position on the sky, dropping to -3.25 at 75° off the galactic plane. This models will no doubt increase in complexity as higher resolution maps are made. Finally, the increased power in the 94GHz channel is consistent with thermal dust emissions with $\beta \approx 2$ discussed in the next subsection (*Kogut et al.* [2007]).

2.10.2 Thermal Dust Emission

Aspherical dust particles with strong magnetic moments can be aligned to magnetic fields in the interstellar medium, often with their longest axis perpendicular to the fields. As a result, they absorb and emit radiation with a partial polarization perpendicular to the field lines.

Dust emissions are frequently modeled as multiple thermal components with a frequency-dependent emissivity: $I(\nu) \sim \nu^{\beta} B_{\nu}(T)$. While these sources are expected to dominate over synchrotron emissions for frequencies above 100GHz, there is little data cur-
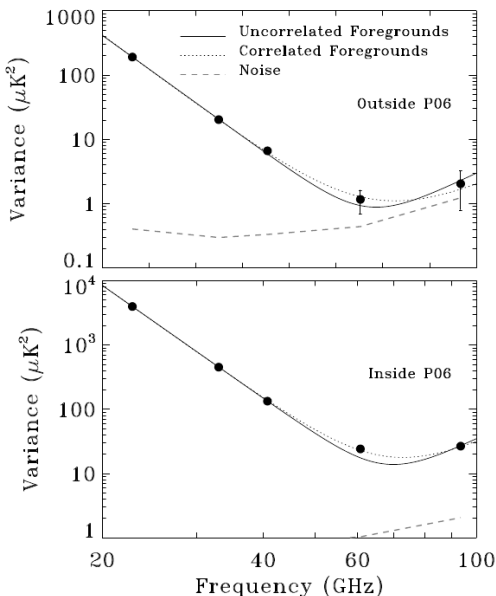
Figure 2.13. Polarized Foreground emissions from WMAP. They are consistent with a synchrotron emissions model with $\beta \approx -3$ except for the two highest frequency channels that are best described with a thermal dust emission model. Note that the foreground contributions decrease off the galactic plane. Graphi from *Kogut et al.* [2007]

rently available in the millimeter range. Data from the COBE satellite's Diffuse Infrared Background Experiment(DIRBE) mapped the sky with 6° resolution at 100 μm and 240 μm (3000GHz and 1250GHz). These maps have been modeled with two components at Temperatures 9.5K and 16K, with β of 1.7 and 2.7 respectively (*Finkbeiner et al.* [1999]). However, the High Frequency Instrument (HFI) on the Plank satellite has six bands between 100GHz and 857GHz, the lowest four of which have polarization sensitivity. This instrument will like provide much more data on this in the near future.

2.11   Conclusions

Recent success in measuring the CMB's temperature and polarization anisotropies have driven the rapid progress in Cosmology over the past decade. There are potentially even greater rewards for those who can successfully separate the B-mode polarization from CMB

maps. However, these signals are extraordinarily weak and will likely be masked by polarized emissions from our own galaxy.

While existing technology has enabled great strides, it is unlikely to suffice for future CMB polarization measurements. As a field, we will need both increased optical through-put in our telescopes coupled with the ability to spectrally differentiate foregrounds from cosmic signals. Absent these motivations, the detector work described in this thesis is still an interesting exercise in electromagnetic design. However, with these cosmological challenges in mind, the novel design methodology may enable otherwise impossible advances in fundamental physics.